Title	A global-local fretting analysis methodology and design study for the pressure armour layer of dynamic flexible marine risers
Author(s)	O'Halloran, Sinéad; Connaire, Adrian D.; Harte, Annette M.; Leen, Sean B.
Publication Date	2019-09-19
Publication Information	O'Halloran, S. M., Connaire, A. D., Harte, A. M., & Leen, S. B. (2020). A global-local fretting analysis methodology and design study for the pressure armour layer of dynamic flexible marine risers. Tribology International, 142, 105967. doi: https://doi.org/10.1016/j.triboint.2019.105967
Publisher	Elsevier
Link to publisher's version	https://doi.org/10.1016/j.triboint.2019.105967
Item record	http://hdl.handle.net/10379/15639
DOI	http://dx.doi.org/10.1016/j.triboint.2019.105967

A global-local fretting analysis methodology and design study for the pressure armour layer of dynamic flexible marine risers

S.M. O'Halloran[a], A.D. Connaire[b], A.M. Harte[c1], S.B. Leen[d1*]

[a] SEAM Research Centre, Waterford Institute of Technology, Waterford, Ireland

[b] Wood Group Kenny, Galway Technology Park, Parkmore, Galway, Ireland

[c] Civil Engineering, National University of Ireland, Galway, Ireland

[d] Mechanical Engineering, National University of Ireland, Galway, Ireland

[1] Joint senior authors

* Corresponding author: Prof. Sean Leen, sean.leen@nuigalway.ie

Abstract

In this paper, a global-local computational methodology for analysis of the pressure armour layer in flexible risers is presented. The methodology consists of a hierarchy of models, including a global riser dynamics model, geometrical and analytical riser sub-models, and an axisymmetric nub-groove local contact model. This, combined with fretting testing of pressure armour material, allows for quantification of key fretting variables, such as contact pressure, relative slip and sub-surface stresses in this complex geometry, under representative loading conditions. The key functional relationships between global riser variables (running conditions) and local nub-groove fretting variables are identified. This facilitates identification of the critical riser curvatures for minimum predicted numbers of cycles to crack initiation for different riser design geometries. Furthermore, a weight function method for crack propagation is implemented for various riser geometries, to allow prediction of total fretting fatigue life. Running condition fretting maps for different riser geometries are thus

developed. The resulting predicted fretting fatigue lives are found to be in the same range as tensile armour layer plain fatigue lives.

Keywords: Flexible marine risers, nub-groove contact, crack initiation, fretting wear, fretting fatigue, fretting case study

1 Introduction

Fretting is a surface damage mechanism that occurs in bodies in contact under a normal, clamping load and cyclical tangential loading. Fretting contact conditions can be classified according to slip regime [1], depending on the slip amplitude as follows: (i) gross slip (for limiting friction conditions), (ii) partial slip (below limiting friction) and (iii) stick. The slip regime depends specifically on the applied combination of normal (clamping) load and tangential load or displacement. Glaeser [2] reported that billions of dollars could be saved if wear and fatigue life of engineering components could be improved. Since then improvements have been made in the understanding and analysis of fretting wear and fatigue performance of components, such as spline couplings, used in aerospace engineering [3,4], gas turbine dovetail joints [5], steel wire ropes [6] and other industrial applications. Burke and Witz [7] presented an excellent review of the problem of fretting in the pressure armour wire of flexible marine risers at an oil and gas industrial conference. Despite this, the problem of fretting fatigue in flexible marine risers has received relatively little attention.

Flexible marine risers are vital infrastructure in the delivery of offshore oil and gas from well-heads at the seabed to a floating vessel or platform at sea level. The key engineering design of these risers is the large number of layers (see Figure 1) with different functions, giving flexibility and strength to withstand substantial sea-state loading conditions. Fretting is

a key concern in the design of the pressure armour layer of flexible marine risers, due to the combination of extreme global dynamic loading conditions and the local geometrical and tribological conditions in the nub-groove contact regions (see Figure 1). The primary function of this interlocked metallic layer is to contain internal pressure by resisting hoop stresses. In the case of pressure armour layers, the normal load is primarily due to internal and external fluid pressures (hydrocarbon and hydrostatic) and the tangential load (displacement) is due to bending moment, axial load, torque or a combination of all three, due to vessel motions, wave and current effects on the riser deformation. Fretting wear and fatigue can cause local cracking and damage of the pressure armour layer, thus reducing the service life of the riser. However, the relationship between global riser loading conditions, such as internal and external pipe pressure, vessel motions, wave and current loads, and local nub-groove fretting conditions, such as contact pressure and contact slip is unknown. Perera et al. [8] presented an experimental method for fretting of the pressure armour layer of unbonded flexible pipes. Féret and Bournazel [9] presented a theoretical approach to calculate stresses, contact pressures and slip between tensile armour layers of flexible pipes under axisymmetric loading; however, this approach is not applicable to the pressure armour layer. In this work, a step is taken towards quantifying this relationship by developing a global-local fretting methodology for risers and applying it to realistic riser configurations and sea state loading conditions.

Previous work by the authors has shown that coefficient of friction has a significant effect on predicted trailing-edge tensile stresses in the nub-groove contact of pressure armour layer and, hence on fretting crack initiation in risers [10,11]. A combined fretting wear-fatigue finite element model was developed using an adaptive meshing technique and the effect of bending-induced slip characterised [11,12]. It has been shown that nub-groove contact pressure and bending-induced axial displacement significantly affect predicted crack

initiation. It has also been shown that a surface damage parameter combined with a multiaxial fatigue parameter can accurately predict the beneficial effect of fretting wear on fatigue predictions [12].

A framework for fretting analysis of the pressure armour wire of flexible marine risers has been previously outlined [13]. This design framework is further developed here and a design study for a flexible riser jumper is conducted. Figure 1 shows the design framework implemented in this paper for service life prediction of the nub-groove contact in the pressure armour layer of a flexible riser jumper. A global-local computational methodology, with inputs from an experimental test regime, for analysis of the pressure armour layer in flexible risers is presented. The methodology consists of a hierarchy of models, including a global riser dynamic model, geometrical and analytical riser sub-models, and an axisymmetric nub-groove local contact model. The contact conditions, i.e. coefficient of friction and wear coefficient, in the local model are identified experimentally. Fretting testing of pressure armour material under representative loading conditions are conducted using a recently developed fretting rig. The representative loading conditions are determined from a combination of global riser models and geometrical and analytical riser sub-models, as depicted in Figure 1. Experimental testing of the pressure armour material under representative loading conditions allows for quantification of key fretting variables, such as coefficient of friction and wear rate, which, in turn, control contact pressure evolution, relative slip and sub-surface stresses in this complex geometry.

Running condition fretting maps are developed for the riser jumpers, representing the key functional relationships between global riser variables and the local nub-groove fretting variables. These maps facilitate identification of the critical riser curvatures for minimum predicted numbers of cycles to crack initiation, applied here for different riser design geometries of the design study. The methodology provides crack initiation and propagation

predictions for the range of riser geometries using the three-dimensional critical-plane Smith-Watson-Topper (SWT) multiaxial fatigue indicator parameter and a weight function method, respectively.

2 Methodology

Figure 2 shows the framework for the methodology implemented in this paper. Global and local analyses are combined to predict the fretting fatigue life of the pressure armour wire nub-groove contact. The global analyses are conducted using the finite element software code Flexcom [14–19], to predict dynamic riser response, such as time histories of axial tension, $F(t)$, and riser curvature, $\kappa(t)$, in response to dynamically-imposed vessel motion and sea-state loading conditions. Geometrical and analytical models are used to identify the local FE (axisymmetric) riser model loading conditions, specifically applied displacement, $\Delta_{app}(t)$, additional pressure $p_a(t)$, based on global riser curvature, $\kappa(t)$, and axial tension, $F(t)$, respectively, as shown in the flowchart of Figure 2. Local nub-groove fretting contact is analysed using an FE axisymmetric model, as described previously by the authors [10]. Fretting fatigue life is predicted from the resulting contact stresses, slips and surface traction results using the D_{fret}-SWT parameter, also previously presented by the authors [12]. Hence, wear is not explicitly modelled, thus reducing the computational time for local fretting analysis. Crack propagation is estimated using a weight function approach and hence, total life is obtained for the fretting regions of the risers.

3 Global Riser Analysis

3.1 General

This study focuses on a single line hybrid riser (SLHR) with a flexible riser jumper connecting to a floating production, storage and offloading vessel (FPSO) as shown schematically in Figure 3; three different dynamic flexible riser jumper geometries (internal diameters) are analysed (see Table 1). The water depth from the seabed to MSWL (mean sea water level, as shown in Figure 3) is 2030 m. This is close to the boundary between what is considered to be deep and ultra-deep (> 2,133 m) drilling. As oil reserves in shallower waters deplete, the oil and gas industry are pushed to extract oil at depths once considered too deep for hydrocarbon exploration and extraction. The configuration of SLHR with riser jumpers is often used to extract hydrocarbons at ultra-deep seas. The flexible riser jumpers fully decouple the SLHR from vessel motions; the vessel motions, in turn, are decoupled from the wellhead at the seabed, making hydrocarbon extraction safer.

Cyclic loading of dynamic flexible risers due to wave and current loading induce axial tension and curvature variations along the risers, leading to micro-scale motion between nub-groove contacts in the pressure armour wires. The full study of the behaviour of the flexible dynamic jumpers requires the consideration of long-term cyclic loading.

3.2 Riser configuration and geometrical properties

The FPSO and SLHR hang-off points are typically critical sections for fatigue along the flexible riser due to the high tensions and curvature variation. The sag bend location can also be critical for fatigue also, due to the high curvature variation in this area. However, the full length of the risers is analysed here since critical fretting conditions (PS) may not necessarily coincide with the locations of maximum loading or displacement.

For the three flexible riser jumper geometries (11 inch, 9 inch and 6 inch) investigated here, the inner diameter is based on the required capacity and internal pressure of the riser. The external diameter is used for calculation of drag and buoyancy of the riser. The internal diameter and pipe mass are used to calculate the buoyancy contribution of the internal fluid; the pipe mass also influences the resultant axial force. The internal fluid properties (density and internal pressure) for each riser jumper are also provided in Table 1. These fluid densities and pressures correspond to fluids that are typical of offshore oil and gas extraction, such as water and gas injection. Other geometric properties used for the global riser analysis are provided in Table 2. The external (hydrostatic) pressure, which is dependent on water-depth, and therefore, location along the riser, is zero at the FPSO hang-off; at the SLHR hang-off point, external hydrostatic pressure is 2 MPa.

The submerged sections of the risers experience hydrodynamic forces due to the environmental loading [20]. Generally, drag forces dominate for extreme waves and inertia forces are dominant for smaller waves. Drag and inertia coefficients of 1.2 and 1.8, respectively, are included in the global analysis for all riser geometries.

3.3 Vessel and environmental loading

The vessel motions due to the wave action are modelled using vessel response amplitude operations (RAOs). The motion of all points on the vessel are calculated using rigid body dynamics from a reference point (typically vessel center of gravity) and the associated RAOs. A vessel has six degrees of freedom, three translational and three rotational, as shown in Figure 3. The RAO data for all six degrees of freedom used for this study were obtained from a database of typical FPSO data for this type of riser configuration and sea conditions (courtesy of Wood plc.).

A piecewise linear current profile is used to model the horizontal current velocity distribution that can vary in magnitude and direction with depth. For this study, the direction of the current is assumed to be constant, 0° from the *y*-axis (see Figure 3).

The riser system is subjected to six sea state (regular Airy wave) load cases defined by wave height and period (as shown in Table 3). These wave heights and periods are representative of extreme dynamic loading on the flexible riser jumper from swell and sea wave conditions (Wood plc. met-ocean data). A riser can experience up to 10^6 cycles of each load-case in a year of operation. All wave directions are the same, except for load case 1, where the wave direction is at 90° with respect to the other load cases. This allows for the effect of wave direction to be considered, by comparing load cases 1 and 3.

4 Global-local conditions

4.1 General

This section describes analytical and geometrical models employed to establish global-local relationships for (i) global axial force to local nub-groove contact pressure and (ii) global riser curvature to local nub-groove slip, as shown in the flowchart of Figure 2.

To the author's knowledge, there are no existing methods to identify nub-groove fretting conditions, in particular, contact slip, based on global riser dynamic analysis results. The work of Burke and Witz (1995) identified fretting as a damage mechanism in the nub-groove contact region. Although this work reviewed the issue of fretting in detail, the nub-groove contact loading conditions were not quantified. Perera et al. (2007) performed fretting wear tests on pressure armour wire to quantify the fretting behaviour; however, the loading conditions used were not based on global riser analysis. Féret and Bournazel (1987) presented

a theoretical approach to calculate stresses, contact pressures and slip between tensile armour layers of flexible pipes under axisymmetric loading. Since the pressure armour layer nub-groove articulations are driven by global riser curvatures rather than axisymmetric loading conditions the theoretical approach used by Féret and Bournazel (1987) cannot be used for pressure armour layer nub-groove contacts. The aim of this section is to quantify the global-local response and, hence, provide data for the formulation of material response fretting maps (MRFM) and running conditions fretting maps (RCFM).

4.2 Global riser axial tension

A key design criterion for flexible risers is the avoidance of compressive buckling. Each layer in a flexible riser has a specific function. The function of the tensile armour (wire) layers is to support the axial tensile forces experienced by the riser. The lay angle of the helical tensile armour layer is typically between ±30 and $\pm 40^0$ to the longitudinal axis of the riser; therefore, tensile forces on this layer cause the wires to straighten slightly. This straightening causes pressure on layers under the tensile layer, such as the pressure armour layer. Therefore, global axial tensile force causes additional external pressure on the pressure armour layer, p_a, which can be expressed as follows [21]:

$$p_a = \frac{m\left(\frac{F_w \sin^2(\alpha)}{R_w \cos(\alpha)}\right)}{2\pi R_{pa}} \tag{1}$$

where m is the number of tensile armour wires in the tensile armour layer, F_w is the axial force in each tensile armour wire, R_w is the radius at which the tensile armour layer lies with a lay angle of α and $2\pi R_{pa}$ is the circumference of the pressure armour layer. This analytical solution has been validated and used extensively, e.g. [22,23].

4.3 Global riser curvatures

In this section, a geometrical model is presented to relate global riser curvature-applied displacement for a local FE model of the riser nub-groove contact, as outlined in Figure 2, is described. In order to develop this model, some assumptions are made, as follows:

- Plane sections remain plane
- The outer pressure armour layer slides relative to the inner layer under bending
- No ovalisation of the riser occurs under bending
- The angle of rotation, θ, remains small ($R\theta \approx l$, see Figure 4)
- The length of riser modelled, l, is small with respect to the bend radius, R
- Pure bending occurs about the centre line of the riser
- Only elastic behaviour occurs (i.e. plasticity is neglected)
- No additional nub-groove contact pressure occurs due to riser bending

The length of the riser section modelled, l, in the simplified axisymmetric model is 15 mm, as described below, and the minimum bend radius of a riser is typically 1.5 to 3 m (this is the storage radius of the pipe - the bend radius during operation is much larger). Therefore, the angle of rotation, θ, remains small (maximum 0.3^0 to 0.6^0), and the section of the riser modelled is small compared to the bend radius (~ 1 %). A schematic of the geometrical model used to develop the riser curvature-applied displacement, κ-Δ_{app}, relationship is shown in Figure 4, where curvature κ, is given by the inverse of bend radius, R.

From the geometrical construction (model) of Figure 4, the angle of rotation, θ, can be expressed in terms of riser bend radius, R, and length of riser section modelled, l, as follows:

$$\theta \approx 2\,sin^{-1}\left(\kappa\frac{l}{2}\right) \tag{2}$$

where l is as shown in Figure 4. Assuming that the outer pressure armour layer slides as a rigid body relative to the inner layer, the relative applied displacement, Δ_{app}, can be approximated as follows, for small θ:

$$\Delta_{app} \approx \pm y\theta \tag{3}$$

where y is the distance from the central riser axis to the nub-groove interface, as shown in Figure 4.

5 Local nub-groove analysis

5.1 Experimental characterisation of fretting of pressure armour material

A custom fretting test rig was developed and designed to measure coefficient of friction and quantify fretting behaviour of materials, in particular, pressure armour wire material [24]. Figure 5 shows the labelled fretting rig. The main components include crossed-cylinder specimen configuration, a linear drive line with a piezoelectric actuator to produce reciprocating displacement and a collet to fix the test specimen in place, dead weight normal loading and displacement sensor (DVRT) and force sensors connected to a PC via a data acquisition unit.

The use of a piezoelectric actuator allows for closed-loop controlled cyclical displacements of ± 1 to 15 μm and a maximum tangential force of 172 N (resulting in typical of riser nub-groove contact pressures of 700 to 1700 MPa). A piezoelectric force sensor and DVRT are used to measure the tangential force and displacement, respectively. A LabView program has been developed to allow for simultaneous actuator control and data acquisition to take place.

Fretting experiments were conducted on pre-drawn pressure armour, pearlitic steel material [25] using the newly-designed fretting test rig [24]. This material has the same chemical composition as the riser material; however, the microstructure is different to that of the cold formed pressure armour wire profile. A crossed cylinder specimen configuration was used, as shown in Figure 5. This configuration allows high contact pressure tests to be conducted, representative of nub-groove contact pressures. The specimens were ground giving a roughness (*Ra*) of 0.4 to 0.7 μm. The test methodology employed was based on ASTM standard test methods [26,27].

A dead-weight configuration was used to provide a constant normal load, *P*, throughout the test. This displacement, Δ^*, throughout the test is also measured at a location as close as possible to the contact using a DVRT. Similarly, the tangential force is measured using a piezoelectric force sensor. The load and displacement signals are sampled at a rate of 250 per fretting cycle for all the experiments (i.e. 500 Hz).

Real-time visualisation of sensor outputs allows for continuous monitoring of the fretting contact behaviour. This data is processed to give fretting loop evolution for each test; idealised gross-slip and partial-slip fretting loops are shown in Figure 6. The measured displacement amplitude (at the DVRT), Δ^*, is not the same as the contact slip due to elastic deformation of the specimen and rig compliance. Since the fretting contact region is separated from the location of the displacement sensor, the measured displacement amplitude, is always slightly larger than the contact slip amplitude, δ^*; this is due to elastic deformation of the specimen and rig compliance. The contact slip amplitude (δ^*) can be derived by measuring the displacement at zero force, as illustrated in Figure 6.

Traditionally, the coefficient of friction (CoF) used by researchers was based on the Coulomb-Amontons' friction law. This method is applicable for an idealised experimental fretting loop, as indicated in Figure 6(b), with CoF given by:

$$CoF = \frac{Q^*}{P} \tag{4}$$

where Q^* is the measured tangential (frictional) force during sliding and P is the applied normal load.

Fouvry et al. [28] observed that the tangential force does not remain constant through the sliding part of the fretting loop, as illustrated in Figure 6(c). It was suggested [28] that the peaks at the end of each sliding section of the fretting loops are caused by ploughing, which occurs during fretting when material build-up occurs at the wear scar edges. To minimise the influence of the ploughing effect on calculation of CoF, Fouvry et al. [28] proposed that the energy dissipated per cycle could be used to define a coefficient of friction which is more representative of the overall behaviour of the contact. The energy coefficient of friction (ECoF) [28] is defined as follows:

$$ECoF = \frac{E_d}{4P\delta^*} \tag{5}$$

where E_d is the dissipated energy per cycle (area of the fretting loop, see Figure 6 (c)) and $4\delta^*$ is the total sliding distance per cycle [28]. The maximum contact slip, δ^*, can be derived by measuring the displacement at zero force, as illustrated in Figure 6. For partial slip, tractional coefficient is used, which is given by *ECoF* for a PS fretting loop shown in Figure 6(a).

Experiments were conducted for a range of normal loads, P. A summary of the fretting test parameters is provided in Table 4. Tests were conducted at ambient temperature (typically ~20 °C), at a frequency of 2 Hz for a duration of 300,000 cycles. Using Young's modulus of

189 GPa and a Poisson's ratio of 0.33 for this steel, Hertzian contact mechanics [29] for a crossed-cylinder contact was used to determine the initial contact semi-width, a, and initial maximum contact pressure, $p_{o.}$ The values of a and p_o are also presented in Table 4. Contact semi-width ranges from 80 μm to 157 μm and maximum contact pressure ranges from 890 MPa to 1730 MPa.

Figure 7 presents the measured evolution of the traction coefficient with number of fretting cycles for crossed-cylinders under different normal loads. The development of ECoF for gross slip fretting is presented in Figure 7(a); the stabilised ECOF values range from 0.59 to 0.65 in GS. Higher normal loads give lower ECoF values, resulting in partial slip conditions. The development of traction coefficient for partial slip fretting is presented in Figure 7(b). The traction coefficient for a normal load of 43 N (contact pressure ~ 1350 MPa) shows a step down from about 0.52 to about 0.42 at about 10^3 cycles; this is consistent with the MS fretting loops shown in Figure 8 (b). In partial-slip, the stabilised traction coefficient value was found to reduce with increased normal load, as expected.

Measured fretting loop evolutions for (a) GS, (b) MS and (c) PS conditions are presented in Figure 8. Gross slip loops are observed for the low contact pressure (1270 MPa); partial slip occurs at higher contact pressure (1600 MPa). Mixed-slip fretting loops are observed for the test conducted with a contact pressure of 1350 N (Figure 8 (b)).

5.2 Finite element analysis of nub-groove contact conditions

Following global-local riser geometric analysis, combined with experimental nub-groove fretting characterisation, the local nub-groove slip, δ, is identified as a function of applied riser displacement, Δ_{app}, from the axisymmetric riser model of Figure 9. The pressure armour wire of a flexible pipe is helically wound at an angle of approximately 5° to the

circumferential direction of the pipe, i.e. approximately circumferential to the pipe. Hence, it is assumed that the helix angle of the pressure armour wire can be ignored for the purpose of these simulations, so that the riser can be modelled as axisymmetric. Furthermore, a repeated axial segment of the riser pressure armour wire was modelled to reduce computational time (see Figure 9).

A detailed mesh refinement study was carried out to ensure convergence with respect to contact variables and substrate stresses in the nub and groove region. The convereged element dimensions in the contact region are 2 μm × 2 μm. Four-node bilinear axisymmetric quadrilateral elements (CAX4) are used. The master-slave algorithm with finite sliding contact within Abaqus was used to define the surface interaction for both models. The maximum allowable penetration depth between master and slave nodes was set to 1 μm. The adjustment tolerance for the initial geometry was set to 0.001 μm. Since the Coulomb-Amontons' law is assumed for sliding friction, the exact stick condition is ensured by implementing Coulomb friction based on the Lagrange multiplier contact algorithm. Further model details are outlined in [10].

In this study, the internal and external pressure for the riser are outlined in Table 1; the additional pressure due to the straightening of the tensile armour wires, p_a, given by Equation (1), is also modelled. The cyclic applied displacement, $\pm\Delta_{app}$, is identified by substituting $\Delta\kappa$ for κ in Equations (4) and (5), where the global curvature range, $\Delta\kappa = \kappa_{max} - \kappa_{min}$, where κ_{max} and κ_{min} are the maximum and minimum curvatures that occur at a specific point on the riser throughout the dynamic simulation. The riser curvature histories in this study are typically symmetrical about the neutral axis of the riser (see Results section and Figure 10).

5.3 Crack initiation

The numbers of cycles to crack initiation (10 μm crack) have been calculated using the methodology outlined in [12]. This implements the fretting damage parameter proposed by Ding et al. [30], D_{fret}, along with critical-plane SWT fatigue indicator parameter for the nub-groove fretting contact in flexible marine risers as outlined in Figure 2. Therefore, wear is not explicitly modelled here. The D_{fret} method introduces a surface damage factor for the effects of fretting wear in conjunction with critical-plane SWT approach, developed to incorporate the effects of slip and surface wear damage on crack initiation, as follows:

$$\sigma_{\max}\Delta\varepsilon_a D_{fret} = \frac{(\sigma'_f)^2}{E}(2N_i)^{2b} + \sigma'_f\,\varepsilon'_f\,(2N_i)^{b+c} \tag{6}$$

where

$$D_{fret} = (1 - C\tau\delta)\left\langle 1 - \frac{\tau\delta}{(\tau\delta)_{th}}\right\rangle^m \tag{7}$$

where C, m, and $(\tau\delta)_{th}$ are material parameters; τ and δ are the local contact shear and slip, respectively. $(\tau\delta)_{\text{th}}$ has been estimated here as a value slightly greater than the value at the partial slip-gross slip transition, based on FE simulations and following Ding et al. [30]. For $\tau\delta < (\tau\delta)_{\text{th}}$, the unmodified SWT value is used (i.e. $D_{\text{fret}} = 1$); for $\tau\delta > (\tau\delta)_{\text{th}}$, the SWT-$D_{\text{fret}}$ value is used [10].

5.4 Crack propagation

This section describes the estimation of crack propagation using a weight-function approach [31], as outlined in Figure 2. The total fretting fatigue life can then be calculated as the sum of crack initiation and propagation lives. The weight function approach was used for the PS regime, where it is assumed that wear rate is low and therefore, wear has little or no effect on

substrate stresses. Since wear is not explicitly modelled, the contact stress gradient in the nub-groove contact region is expected to reduce up to a depth where constant stress is observed (far from the nub-groove contact surface). In an attempt to capture the effect of fretting stress relaxation due to wear, stress reduction factors have been estimated based previously presented stress relaxation trends perpendicular to the contact surface due to wear [24]. These estimated stress gradients have been used here to estimate crack propagation in the gross-slip regime.

The weight function method used for PS is described below. In fretting experiments, cracks have been observed to grow at a shallow angle initially, typically between 5^0 and 20^0 [32], being influenced by the contact load. The crack will grow in this manner for up to three microstructural grain sizes [33]. Next the direction of the crack propagation changes to approximately perpendicular to the contact surface; here the propagation direction is influenced by the bulk stress in the pressure armour wire [24].

Due to stress gradients close to the contact surface in fretting, crack propagation is a complex issue [34]. Houghton et al. [31] used weight functions based on the work of Nicholas et al. [35] to analyse the mixed-mode cracking of Ti-6Al-4V to predict multiaxial fretting fatigue. Crack location was found from SWT critical plane calculations, and local stress ranges were identified for Mode I and Mode II crack propagation. The weight functions, h_{I} and h_{II}, for Mode I and Mode II crack growth, respectively, are defined as [36]:

$$h_I = \sqrt{\frac{2}{\pi a}} \frac{1}{\sqrt{1-\rho}} \left[1 + \sum_{\upsilon,\mu} \frac{A_{\upsilon,\mu} \alpha^{\mu}}{(1-\alpha)^{\frac{3}{2}}} (1-\rho)^{\upsilon+1} \right] \tag{8}$$

$$h_{II} = \sqrt{\frac{2}{\pi a}} \frac{1}{\sqrt{1-\rho}(1-\alpha)^{\frac{1}{2}}} \left[(1-\alpha)^{\frac{1}{2}} + \sum_{\upsilon,\mu} A_{\upsilon,\mu} (1-\rho)^{\upsilon+1} \alpha^{\mu} \right] \tag{9}$$

where $\rho = x/a$ and $\alpha = a/W$, a is the crack length, x is the distance along the crack, W is the specimen width and $A_{\upsilon,\mu}$ is the influence coefficient for each weight coefficient [36]. Mode I and Mode II stress intensity factors are defined as:

$$\Delta K_I = \int_0^a \Delta\sigma_{xx}(x) h_I(x,a) dx \tag{10}$$

$$\Delta K_{II} = \int_0^a \Delta\sigma_{xy}(x) h_{II}(x,a) dx \tag{11}$$

where $\Delta\sigma_{xx}$ and $\Delta\sigma_{xy}$ are the local FE-predicted normal and shear stresses during crack growth in Mode I and Mode II, respectively. The effective stress intensity factor is:

$$\Delta K_{eff} = \sqrt{\Delta K_{I,eff}{}^2 + \Delta K_{II,eff}{}^2} \tag{12}$$

where:

$$\Delta K_{I,eff} = \Delta K_I (1-R)^{(1-n)} \tag{13}$$

where R is the stress ratio > 0 and n is a material constant, where $0 < n < 1$. In this work, n was chosen to be 0.5. The incremental crack growth, Δa, is defined by:

$$\Delta a = C(\Delta K_{eff} - \Delta K_{th})^m \Delta N \tag{14}$$

where ΔN is a cycle jumping factor. The process crack growth calculation is incrementally repeated until the crack length, a, propagates to a length of 2 mm; at this distance away from the contact region, the primary stress is in the axial direction. Previously published Paris coefficients for a dual phase pearlite-ferrite cold-formed steel were used here [37]. This methodology has been successfully validated against results obtained from the Paris equation for a plane fatigue case. This method includes the El-Haddad correction for short crack growth [38].

6 Results

6.1 Global analysis

Key output variables from the global analysis are (i) time histories of riser curvature and axial tension and (ii) envelopes of the minimum and maximum riser curvatures and axial tensions along the length of the riser. This data allows for detailed design of flexible risers based on dynamic responses to various sea state loadings.

Normalised time histories of resultant rise curvature (κ/κ_{max}), axial tension (F/F_{max}) and internal and external pressures (p/p_{max}) results from dynamic riser analysis are shown in Figure 10; these results are for the SLHR hang-off point. The internal and external pressure remain constant with respect to time. In all load-cases, riser curvature is seen to be 180^0 out of phase with axial tension. The axial force is tensile at all times.

The minimum and maximum axial force and riser curvature along the length of the 6 inch riser under load case 1 are presented in Figure 11. Note that l in these plots is the length of the riser, measured as curvilinear distance along the riser from the FPSO hang-off point (see Figure 3). The end-point (l = 550 m) corresponds to the SLHR hang-off point. Clearly, the predicted location of maximum axial tension and riser curvature values is at the SLHR hang-off point. The SLHR has a more dynamic response to the sea-state loading than the FPSO, therefore, the SLHR hang-off point is the most dynamically loaded point on the flexible riser. The results from the other load-cases analysed for the three risers are consistent with these.

6.2 Global-local loading conditions

A typical predicted relationship between nub-groove contact displacement (δ) and riser curvature range ($\Delta\kappa$) from FE analysis is shown Figure 12. This response is obtained from the

global riser curvature results, Equations (4) and (5) and the local FE riser model (Figure 9). The curvature-slip response shows two types of trends depending on slip regime, for finite sliding friction; a quadratic trend is observed for PS and a linear trend is observed for GS. To achieve slip, i.e. overcome friction, a certain threshold curvature range, $\Delta\kappa_{th}$, is required; above this threshold value, curvature-slip response is much "softer", i.e. a smaller change in curvature results in a larger change in slip. The value of $\Delta\kappa_{th}$ depends on riser geometry and loading conditions.

This combined geometrical-axisymmetric FE method, as described in Figure 2, has been compared to the 3D riser model presented in [24] (see Figure 12). This model, however, by necessity, uses a much coarser local contact mesh. The general trend is seen to be the same. Differences are attributed to the simplifying assumption of axisymmetry and the coarser mesh for the 3D riser model. The analysis of curvature-slip relationship requires further computational investigation and full-scale experimental validation, if possible.

Figure 13 shows the curvature-slip relationship for the different size risers. Again, the effect of decreasing riser diameter is the same as that of increasing internal pressure and increasing CoF.

Threshold values of curvature range, $\Delta\kappa_{th}$, have been identified as the curvature range at which nub-groove contact transitions from PS to GS.

The $\Delta\kappa$-δ relationships shown above can be described by the following equations, for PS and GS:

$$\delta = A(\Delta\kappa)^2 + B(\Delta\kappa) + C \quad \text{(PS)} \tag{15}$$

$$\delta = B(\Delta\kappa) + C \quad \text{(GS)} \tag{16}$$

where *A*, *B*, and *C* for each riser geometry and nub groove sliding regime are given in Table 5. The values of $\Delta\kappa_{th}$ are also provided in Table 5. Partial slip occurs at $\Delta\kappa$ values less than $\Delta\kappa_{th}$.

The predictive methodology has been applied to the various dynamic load cases for each riser diameter. The results for maximum predicted slip for each riser are shown in Table 6. For the minimum loading conditions along the riser lengths, stick is predicted, whereas for the maximum conditions along the riser lengths, gross slip is typically predicted. Therefore, along the riser length, stick, partial slip and gross slip conditions are experienced for most load cases. Load case 5 results in maximum nub-groove contact displacements closest to PS-GS transition. Typically, the larger wave heights (see Table 3) result in larger nub-groove slips, i.e. load cases 1 to 3; this is due to larger vessel and SLHR motions associated with wave loading, and hence, larger global riser dynamic motions occur compared to load cases with lower wave heights, i.e. load cases 4 to 6.

6.3 Predicted life to crack initiation

Figure 14 presents the predicted number of cycles to crack initiation versus nub-groove displacement for all three risers. At lower contact slips (< 2 μm) the 11 inch riser is most critical (lower predicted life); however, as contact slip increases (> 4 μm), the 6 inch riser is more critical in terms of predicted number of cycles to crack initiation.

Figure 15 presents the effect of riser curvature range, $\Delta\kappa$, on predicted number of cycles to crack initiation for all three risers. The difference between the riser configurations can be clearly seen. The PS regime occurs at much lower curvatures for the larger diameter risers (11 inch and 9 inch) than for the smaller diameter riser (6 inch). This is due to the different curvature-slip relationships for each riser, as shown in Figure 13. Figure 15 is an example of

a RCFM; this can be used to identify the number of cycles to crack initiation from global riser curvature response.

Figure 15 also shows critical curvature range ($\Delta\kappa_{\text{crit}}$) that relate to lower predicted lives ($N_{\text{i}} < 5 \times 10^4$) for each riser. The smaller diameter (6 inch) riser has a large range of $\Delta\kappa_{\text{crit}}$ than the larger diameter risers (9 inch and 11 inch). These $\Delta\kappa_{\text{crit}}$ values can be used in conjunction with global riser analysis results (from global riser analysis) to identify locations of the riser where fretting fatigue cracking are likely to occur. For all load cases, $\Delta\kappa_{crit}$ occurs closest to the SLHR hang-off point (between 0.1 m and 5 m from hang-off point) for each of the risers. It must be noted that these values for $\Delta\kappa_{\text{crit}}$ are specific to each of these risers under the loading conditions outlined above and with a nub-groove CoF of 0.7.

The predicted number of cycles to crack initiation for each load case and riser is presented in Figure 16. The 11 inch riser is typically the most critical riser, in terms of predicted number of cycles to crack initiation, compared to the smaller diameter risers (9 inch and 6 inch). The load case with the most difference between predicted riser lives is load case 5; this corresponds to the load case with the lowest wave height and period. Comparing the predicted number of cycles to crack initiation for load cases 1 and 3 indicates that wave direction has an effect on predicted life; therefore, in a full riser analysis, a full range of wave loading directions should be considered. The location where $\Delta\kappa_{\text{crit}}$ occurs along the riser length is short relative to the length of the riser, typically $\leq$ 2 m compared to overall riser length of 550 m. This is approximately 0.4 % of the riser length that is critical for fretting design.

6.4 Predicted crack propagation

Figure 17 presents the predicted number of cycles to crack initiation and propagation against nub-groove displacement for the 6 inch riser. Estimated propagation life is much longer than predicted initiation life (typically by two orders of magnitude). This is due to the fact that the high fretting stresses are highly localised close to the nub-groove contact surface (shown in Figure 5.7), and therefore, have little influence as the crack propagates. Figure 17 presents the effect of riser curvature range, $\Delta\kappa$, on predicted number of cycles to crack initiation and propagation for the 6 inch riser. Figure 18 presents the effect of riser curvature range, $\Delta\kappa$, on predicted number of cycles to crack initiation and propagation for all risers. This is an example of a RCFM and can be used to identify the number of cycles to failure from global riser dynamic response.

Figure 19 presents the predicted number of cycles to failure for all three risers and all load cases. There is a significant increase in life for all risers and load cases compared to predicted initiation life (shown in Figure 16). There is less scatter between the results for failure than for initiation, indicating that crack propagation is dominant over crack initiation, due to stresses perpendicular to the surface decreasing rapidly with increasing depth into the substrate, resulting in similar predicted propagation lives for all risers and load cases.

Currently, there is no standard procedure for the analysis of fretting in the pressure armour layer. Typically, risers are analysed for fatigue behaviour of the tensile armour layer. For this study, the fatigue life of tensile armour layer has also been predicted using Layercom, a tensile armour layer analytical fatigue predictive tool (Wood plc., Galway, Ireland). Thees analytically predicated lives for the tensile armour layer ranged from 5.9×10^5 to 1.3×10^7. This is a similar range to the total fretting fatigue life predicted for the pressure armour layer in this study (see Figure 19). The load cases investigated here are extreme loading scenarios;

by modelling stochastic sea states, less conservative and more realistic life predictions can be calculated using the same predictive methodologies for both fatigue of the tensile armour layer and fretting fatigue of the pressure armour layer.

7 Conclusions

A global-local computational methodology is presented for fretting fatigue of the pressure armour layer in flexible risers under realistic loading conditions. The methodology consists of a hierarchy of models, including a global riser dynamics model, geometrical and analytical riser sub-models, and an axisymmetric nub-groove local contact model. A new fretting test rig is also presented for representative testing of flexible riser pressure armour contact conditions. The key functional relationships between global riser variables (running conditions) and local nub-groove fretting variables have been developed to facilitate identification of critical riser curvatures for fatigue crack initiation and total life in different riser design geometries. Running condition fretting maps are thus presented for the different riser geometries. The resulting predicted fretting fatigue lives are found to be in the same range as tensile armour layer plain fatigue lives.

The riser design study facilitated new insight into fretting in risers, such as:

- The critical curvature range for partial slip (and hence minimum fretting life) reduces with increasing riser diameter
- Propagation life is predicted to be significantly (two orders of magnitude) longer than initiation life, due to the significant gradient in stress with increasing depth into the armour wire substrate

This study has highlighted the requirement for further investigation into the effect of global riser curvature on local nub-groove contact slip. To quantify this effect, 3D riser modelling including detailed geometry of each layer and contact pressures and slip between layers is required. These 3D models should be validated using full-scale riser testing; this is a difficult task since contact slip is difficult to measure experimentally, especially in the small space within the pressure armour layer. However, it may be feasible to implement displacement or position sensors to measure the effect of riser curvature on pressure armour wire displacement; FE modelling can then be used to predict local nub-groove contact slip. The present work will inform new flexible riser design codes and standards which may allow for reduced safety factors for fatigue design of risers [39].

Acknowledgements

The authors would like to thank the Irish Research Council and Wood plc. for funding of this project through the Enterprise Partnership Scheme (EPSPG/2013/638), the National University of Ireland for funding through an NUI Travelling Scholarship. The authors also wish to acknowledge the support of the NUI Galway Engineering Building technical staff; particularly Mr. Bonaventure Kennedy and Mr. Patrick Kelly.

References

[1] Dobromirski J. Variables of fretting process: Are there 50 of them? Stand Frett Fatigue Test Methods Equip 1992:60-60–7. doi:10.1520/STP25816S.

[2] Glaeser WA. Tribology, the science of combating wear. Battelle, Columbus Division; 1981.

[3] Ding J, McColl IR, Leen SB, Shipway PH. A finite element based approach to simulating the effects of debris on fretting wear. Wear 2007;263:481–91. doi:10.1016/j.wear.2006.12.056.

[4] Wavish PM, Houghton D, Ding J, Leen SB, Williams EJ, McColl IR. A multiaxial fretting fatigue test for spline coupling contact. Fatigue Fract Eng Mater Struct 2009;32:325–45. doi:10.1111/j.1460-2695.2009.01334.x.

[5] Ruiz C, Boddington PHB, Chen KC. An investigation of fatigue and fretting in a dovetail joint. Exp Mech 1984;24:208–17.

[6] Cruzado a., Hartelt M, Wäsche R, Urchegui M a., Gómez X. Fretting wear of thin steel wires. Part 1: Influence of contact pressure. Wear 2010;268:1409–16. doi:10.1016/j.wear.2010.02.017.

[7] Burke RN, Witz JA. NFretting Fatigue of Flexible Pipe Pressure Armour. 3rd Eur. Conf. Flex. Pipes, Unbilicals Mar. Cables - Mater. Util. Cycl. Therm. Load., 1995.

[8] Perera SDR, Fernando US, Sheldrake T, Clements R. An investigation into fretting behaviour in pressure armor wires of unbonded flexible pipes. Vol. 3 Pipeline Riser Technol. CFD VIV, vol. 3, San Diego, California, USA: 2007, p. 363–70. doi:10.1115/OMAE2007-29393.

[9] Féret JJ, Bournazel CL. Calculation of stresses and slip in structural layers of

unbonded flexible pipes. J Offshore Mech Arct Eng 1987;109:263. doi:10.1115/1.3257019.

[10] O'Halloran SM, Harte AM, Connaire AD, Leen SB. Modelling of fretting in the pressure armour layer of flexible marine risers. Tribol Int 2016;100:306–16. doi:10.1016/j.triboint.2016.02.040.

[11] O'Halloran SM, Harte AM, Shipway PH, Leen SB. An experimental study on the key fretting variables for flexible marine risers. Tribol Int 2018;117:141–51. doi:10.1016/J.TRIBOINT.2017.07.032.

[12] O'Halloran SM, Shipway PH, Connaire AD, Leen SB, Harte AM. A combined wear-fatigue design methodology for fretting in the pressure armour layer of flexible marine risers. Tribol Int 2017;108:7–15. doi:10.1016/J.TRIBOINT.2016.10.020.

[13] O'Halloran S, Harte A, Connaire A, Leen S. The Prediction of Fretting Fatigue in the Pressure Armours of Dynamic Flexible Pipes. Offshore Technol. Conf., Offshore Technology Conference; 2016. doi:10.4043/26985-MS.

[14] Lane M, O'Sullivan T, Grealish F, Kavanagh K, Thompson H. Advanced Frequency Domain Analysis Techniques for Steel Catenary Risers. Offshore Technol. Conf., Houston, Texas, USA: 2001, p. 1–14. doi:10.4043/13017-MS.

[15] Lang DW, Connolly A, Lane M, Connaire AD. Advances in Frequency and Time Domain Coupled Analysis for Floating Production and Offloading Systems. Int. Conf. Offshore Mech. Arct. Eng., Halkidiki, Greese: 2005. doi:10.1115/OMAE2005-67396.

[16] O'Brien PJ, Lane M, McNamara JF. Improvements to the convected co-ordinates method for predicting large deflection extreme riser response. Int. Conf. Offshore Mech. Arct. Eng., Oslo, Norway: 2002. doi:10.1115/OMAE2002-28237.

[17] O'Brien PJ, McNamara JF, Lane. Three dimensional finite displacements and rotations of flexible beams including non-equal bending stiffnesses. Int. Conf. Offshore Mech. Arct. Eng., Cancun, Mexico: 2003. doi:10.1115/OMAE2003-37372.

[18] Smith R, Carr T, Lane M. Computational tool for the dynamic analysis of flexible risers incorporating benging hysteresis. Int. Conf. Offshore Mech. Arct. Eng., San Diego, California, USA: 2007. doi:10.1115/OMAE2007-29276.

[19] Connaire A, O'Brien P, Harte AM, O'Connor A. Advancements in subsea riser analysis using quasi-rotations and the Newton-Raphson method. Int J Non-Linear Mech 2015;70:47–62. doi:10.1016/j.ijnonlinmec.2014.10.021.

[20] Flexcom Introductory Manual, April 2014: Wood Group Kenny. n.d.

[21] Lanteigne J. Theoretical Estimation of the Response of Helically Armored Cables to Tension, Torsion, and Bending. J Appl Mech 1985;52:423. doi:10.1115/1.3169064.

[22] McNamara JF, Harte AM. Three-dimensional analytical simulation of flexible pipe wall structure. J Offshore Mech Arct Eng 1992;114:69–75. doi:10.1115/1.2919961.

[23] Hoffman J, Dupont W, Reynolds B. A fatigue-life prediction model for metallic tube umbilicals. Offshore Technol. Conf., 2001. doi:10.4043/13203-MS.

[24] O'Halloran SM. Experimental Characterisation , Computational Modelling and Design Tool Development for Fretting Fatigue and Wear in Flexible Marine Risers. Ph.D. Thesis, Mechanical Engineering, National University of Ireland Galway, 2017.

[25] Ashton P. Micromechanical modelling of size effects in crack initiation with application to fretting fatigue and cold dwell fatigue. Ph.D. Thesis, Mechanical Engineering, National University of Ireland Galway, 2018.

[26] ASTM International. ASTM D4170-10 Standard test method for fretting wear

protection by lubricating greases 2010. doi:10.1520/D4170-10.

[27] ASTM International. ASTM D7594-11 Standard test method for determining fretting wear resistance of lubricating greases under high Hertzian contact pressure using a high-frequency, linear-oscillation (SVR) test machine 2011. doi:10.1520/D7594-11.

[28] Fouvry S, Duó P, Perruchaut P. A quantitative approach of Ti-6Al-4V fretting damage: Friction, wear and crack nucleation. Wear 2004;257:916–29. doi:10.1016/j.wear.2004.05.011.

[29] Hertz H. Über die Berührung fester elastischer Körper. J Fur Die Reine Und Angew Math 1882;1882:156–71. doi:10.1515/crll.1882.92.156.

[30] Ding J, Houghton D, Williams EJ, Leen SB. Simple parameters to predict effect of surface damage on fretting fatigue. Int J Fatigue 2011;33:332–42. doi:10.1016/j.ijfatigue.2010.09.008.

[31] Houghton D, Wavish PM, Williams EJ, Leen SB. Multiaxial fretting fatigue testing and prediction for splined couplings. Int J Fatigue 2009;31:1805–15. doi:10.1016/j.ijfatigue.2008.12.005.

[32] Dubourg M, Lamacq V. Stage II crack propagation direction determination under fretting fatigue loading: a new approach in accordance with experimental observations. Frett. Fatigue Curr. Technol. Pract., West Conshohocken, PA: ASTM International; 2000, p. 436-436–15. doi:10.1520/STP14746S.

[33] Khotsyanovskii AO. Life prediction of titanium and aluminum alloys under fretting fatigue conditions using various crack propagation criteria. Part 1. Experimental and calculation techniques. Strength Mater 2010;42:683–704. doi:10.1007/s11223-010-9256-7.

[34] McCarthy OJ, McGarry JP, Leen SB. Microstructure-sensitive prediction and experimental validation of fretting fatigue. Wear 2013;305:100–14. doi:10.1016/j.wear.2013.05.012.

[35] Nicholas T, Hutson A, John R, Olson S. A fracture mechanics methodology assessment for fretting fatigue. Int J Fatigue 2003;25:1069–77. doi:10.1016/S0142-1123(03)00115-4.

[36] Fett T, Munz D. Stress intensity factors and weight functions. Computational Mechanics Publications, Southhampton; 1997.

[37] Li S, Kang Y, Kuang S. Effects of microstructure on fatigue crack growth behavior in cold-rolled dual phase steels. Mater Sci Eng A 2014;612:153–61. doi:10.1016/j.msea.2014.06.002.

[38] El Haddad MH, Topper TH, Smith KN. Prediction of non propagating cracks. Eng Fract Mech 1979;11:573–84. doi:10.1016/0013-7944(79)90081-X.

[39] API. Recomended practices for flexible marine risers, 17J. 2009.

Figures

Figure 1. Design framework for service life prediction of the nub-groove contact in the pressure armour layer of a flexible riser jumper.

Figure 2. Framework for fretting life prediction in flexible marine risers.

Figure 3. Schematic of SLHR and single riser jumper configuration. and definition of vessel degrees of freedom for RAOs.

Figure 4. Schematic of effect of bending on riser section and the geometrical model used to relate riser curvature to local applied displacement.

Figure 5. Design of fretting rig, without dead weight normal loading showing the crossed cylinder test speciment configuration.

Figure 6. Schematic diagram of an ideal fretting loop in the (a) partial slip regime, and (b) gross slip regime, (c) fretting loop with high tractional force peak at the ends of gross slip.

Figure 7. Measured evolution of ECoF and traction coefficients with number of fretting cycles for specimen with normal load of P for (a) gross-slip (contact pressure between 890 and 1270 MPa), and (b) mixed and partial slip conditions (contact pressure between 1350 and 1730 MPa).

Figure 8. Measured evolution of fretting loop for tests with (a) gross slip conditions (contact pressure of 1270 MPa), (b) mixed slip conditions (contact pressure 1350 MPa), and (c) partial (contact pressure of 1600 MPa).

Figure 9. Axisymmetric riser model.

Figure 10. Time histories of normalised results from dynamic riser analysis.

Figure 11. Envelope of minimum and maximum (a) axial tensile force and (b) riser curvature along the length of the 6 inch riser jumper.

Figure 12. Comparison of geometrical and 3D FE models to obtain curvature-slip relationship for the 6 inch riser with nub-groove CoF of 0.7.

Figure 13. Curvature-slip relationship for the different risers used in this study.

Figure 14. Number of cycles to crack initiation against nub-groove displacement for all three risers.

Figure 15. Number of cycles to crack initiation against dynamic riser curvature for all three risers and definition of $\Delta\kappa_{\text{crit}}$ for each riser case.

Figure 16. Predicted numbers of cycles to crack initiation for all load cases and all three risers.

Figure 17. Effect of (a) nub-groove contact slip and (b) global riser curvature on number of cycles to crack initiation and propagation for the 6 inch riser.

Figure 18. RCFM for predicted number of cycles to failure for dynamic curvature range for all three risers.

Figure 19. Predicted numbers of cycles to failure for all load cases and all three risers.

Tables

Table 1. Riser geometrical and internal fluid data.

Table 2. Riser geometrical data.

Table 3. Definition of regular wave load-cases for design study.

Table 4. Summary of the fretting test parameters.

Table 5. *A*, *B*, and *C* for each riser geometry and nub-groove sliding conditions

Table 6. Maximum nub-groove contact displacements for each riser and load case.

Tables

Table 1. Riser geometrical and internal fluid data.

Riser	Inner diameter (mm)	Outer diameter (mm)	Internal Fluid	Internal fluid density (kg/m^3)	Internal pressure (MPa)
11 inch	279.4	404.5	Water Injection	1100	27.3
9 inch	222.3	336.9	Gas Injection	285	32.4
6 inch	152.4	362.8	Gas Lift	267	27.5

Table 2. Riser geometrical data.

Riser	Bending stiffness, *EI* (Nm^2)	Torsional stiffness, *GJ* (Nm^2)	Axial stiffness, *EA* (N)	Mass (kg/m)
11 inch	13×10^3	134×10^3	125×10^6	279
9 inch	37×10^3	371×10^3	95×10^6	208
6 inch	49×10^3	491×10^3	66×10^6	165

Table 3. Definition of regular wave load-cases for design study.

Load case	Wave height (m)	Wave period (s)
1	2.78	11.5
2	2.36	10.54
3	2.78	11.65
4	1.74	6.94
5	0.93	6.94
6	1.74	14.81

Table 4. Summary of the fretting test parameters.

Test temperature	Ambient (typically 20°C)
Cylinder radii, *R*	6 mm
Displacement amplitudes, *Δ**	1 to 6 μm
Test duration, *N*	300,000 cycles
Normal load, *P*	12 to 90 N
Maximum Hertzian pressure, p_o	890 to 1730 MPa
Initial contact width, *a*	80 to 157 μm
Oscillation frequency	2 Hz
Lubricant	None

Table 5. *A*, *B*, and *C* for each riser geometry and nub-groove sliding conditions

Riser	**A**	**B** (PS)	**C**	**B** (GS)	**C**	$\Delta\kappa_{th}$
6 inch	3.9×10^{3}	7.2	-4.3×10^{-3}	1.1×10^{3}	-9.7	8.9×10^{-3}
9 inch	1.0×10^{3}	11.4	-2.2×10^{-3}	1.7×10^{3}	-8.9	5.5×10^{-3}
11 inch	1.8×10^{4}	18.7	-0.6×10^{-3}	1.9×10^{1}	-0.6×10^{-3}	3.7×10^{-3}

Table 6. Maximum nub-groove contact displacements for each riser and load case.

Load case	**6 inch riser δ_{max} (μm)**	**9 inch riser δ_{max} (μm)**	**11 inch riser δ_{max} (μm)**
1	22.8	83	192.1
2	45.4	65.1	192.1
3	78.1	81.9	188.7
4	40.5	44.6	101.8
5	2.1	3.3	4.4
6	29.2	27.2	87.8

Figures

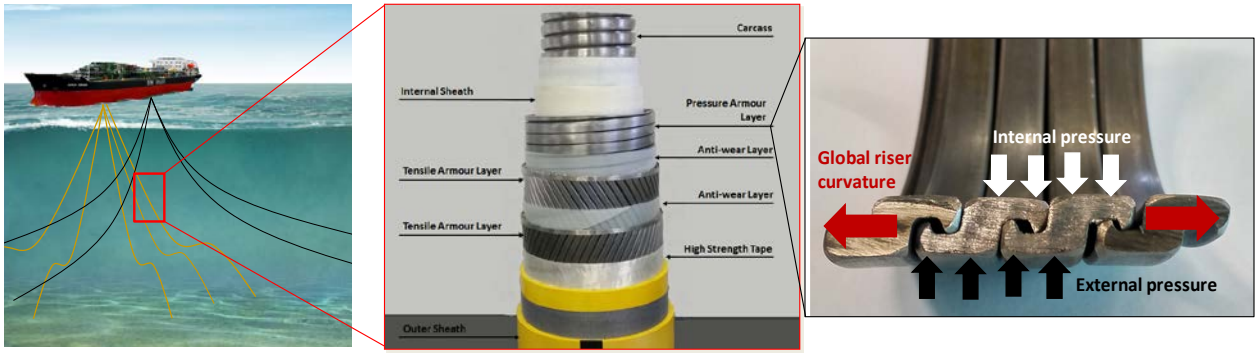

Global riser analysis | Cross-sectional riser analysis | Local nub-groove pressure armour layer analysis

Figure 1. Design framework for service life prediction of the nub-groove contact in the pressure armour layer of a flexible riser jumper.

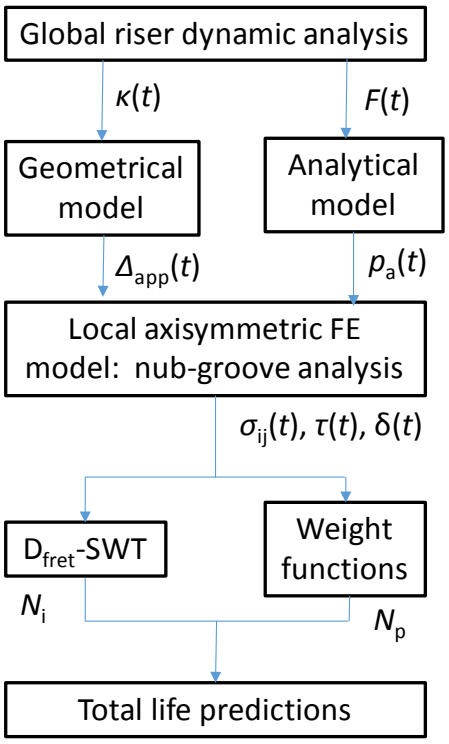

Figure 2. Framework for fretting life prediction in flexible marine risers.

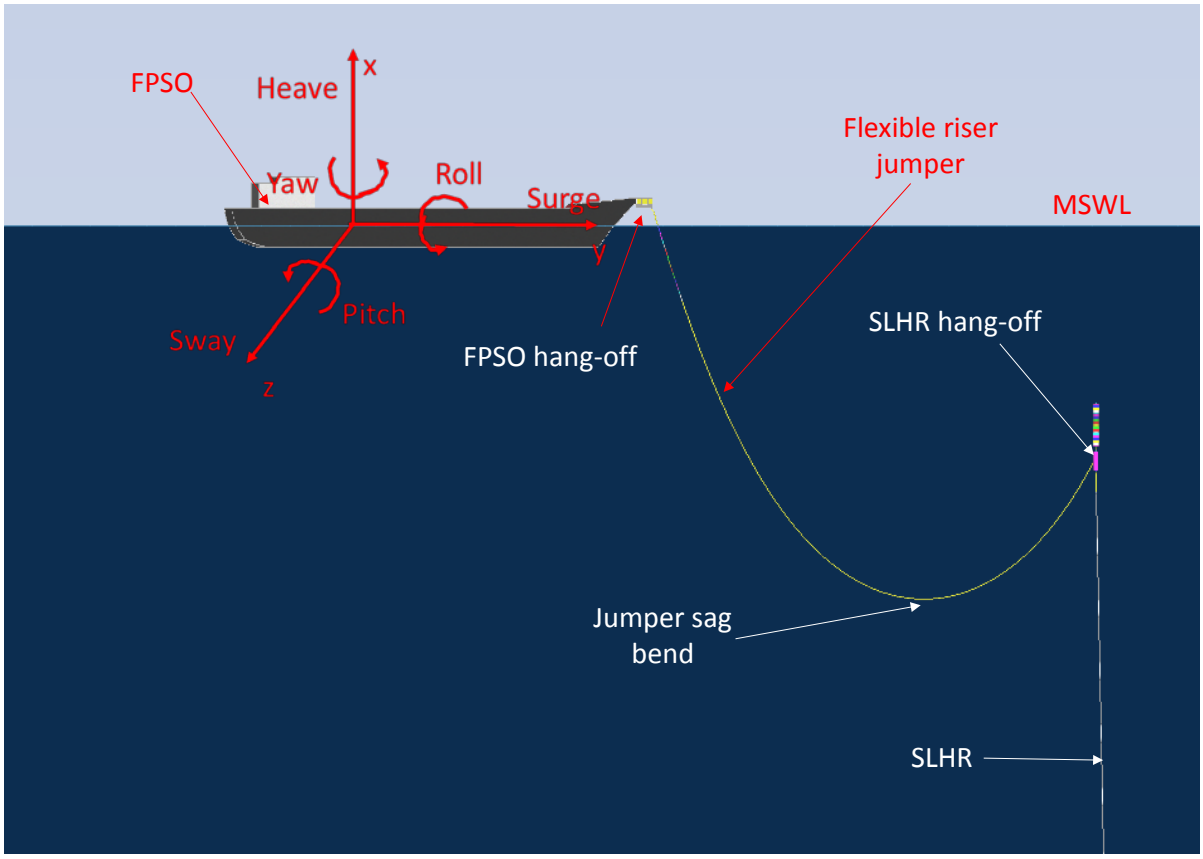

Figure 3. Schematic of SLHR and single riser jumper configuration and definition of vessel degrees of freedom for RAOs.

.

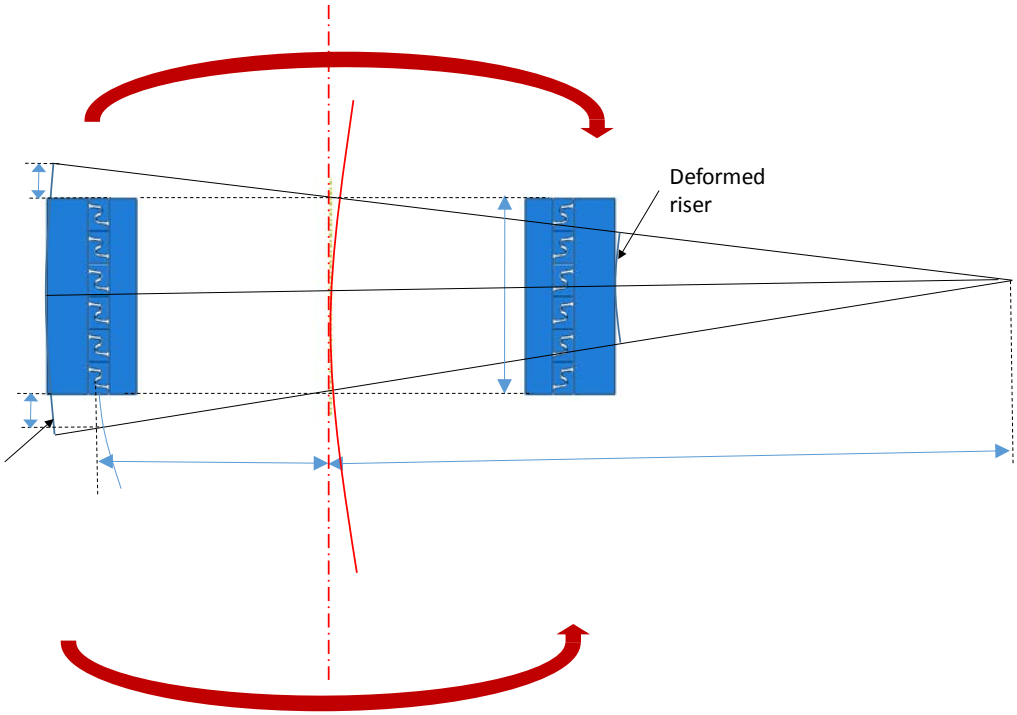

Figure 4. Schematic of effect of bending on riser section and the geometrical model used to relate riser curvature to local applied displacement.

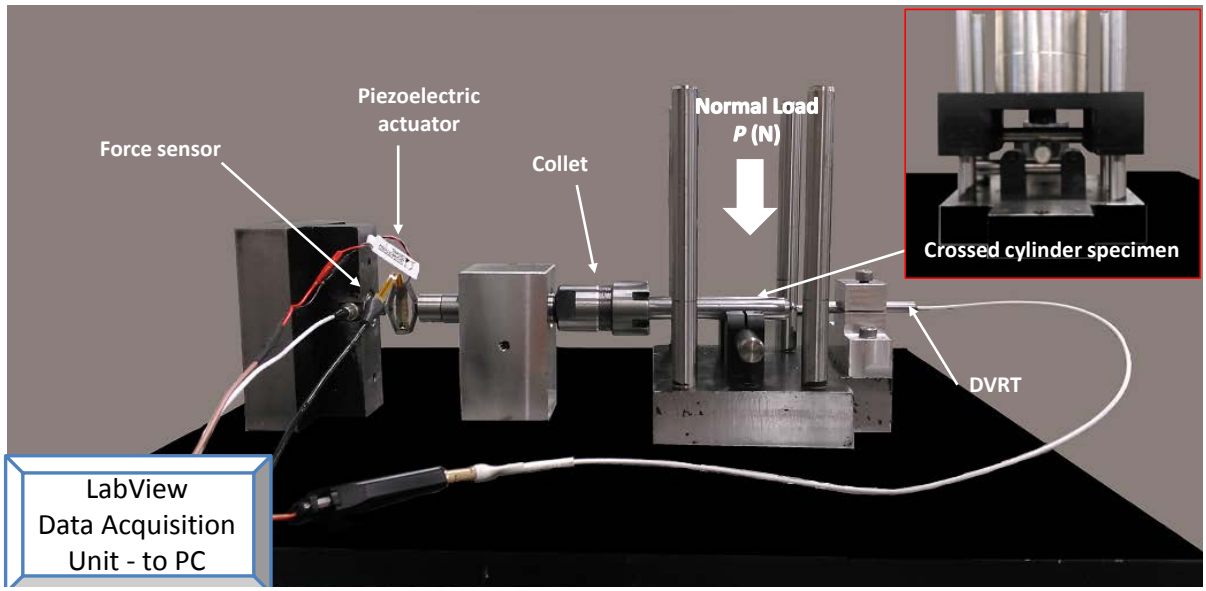

Figure 5. Design of fretting rig, without dead weight normal loading showing the crossed cylinder test speciment configuration.

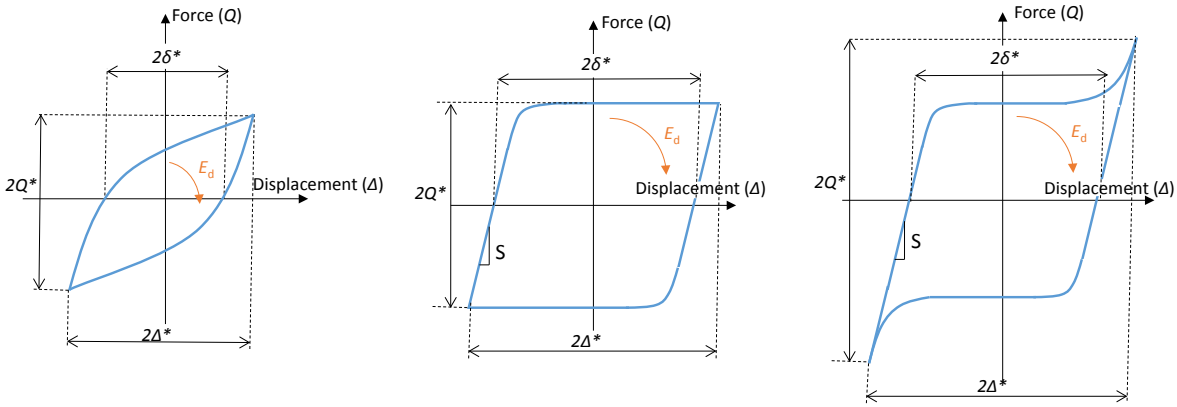

(a) (b) (c)

Figure 6. Schematic diagram of an ideal fretting loop in the (a) partial slip regime, and (b) gross slip regime, (c) fretting loop with high tractional force peak at the ends of gross slip.

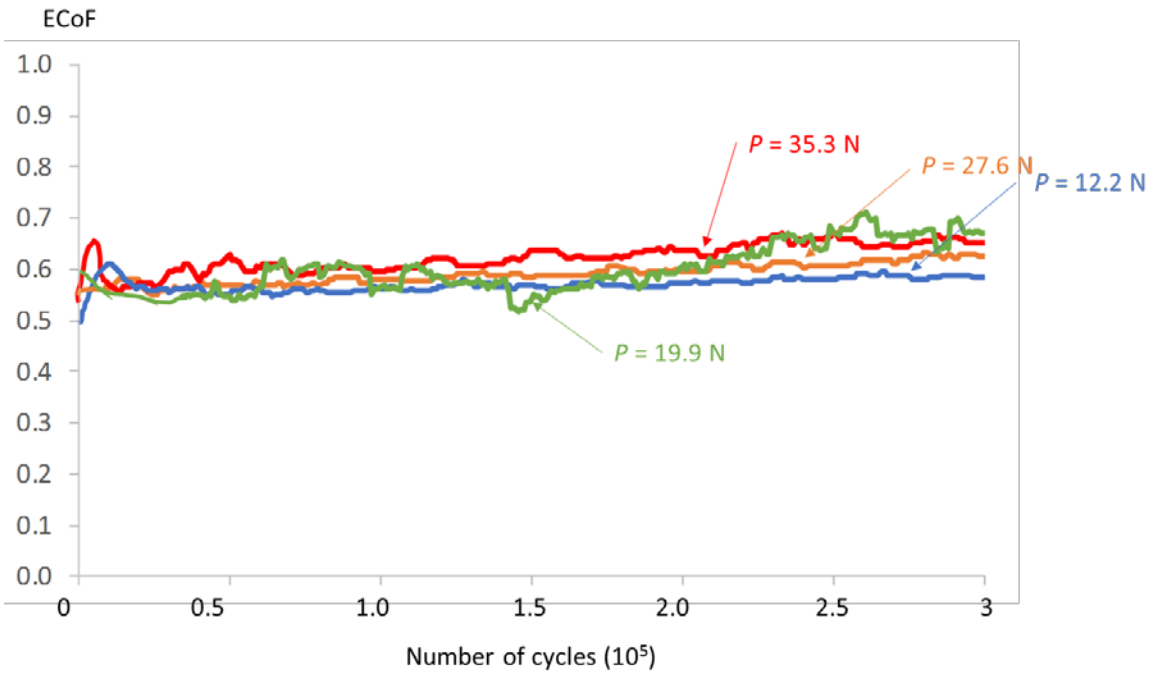

(a)

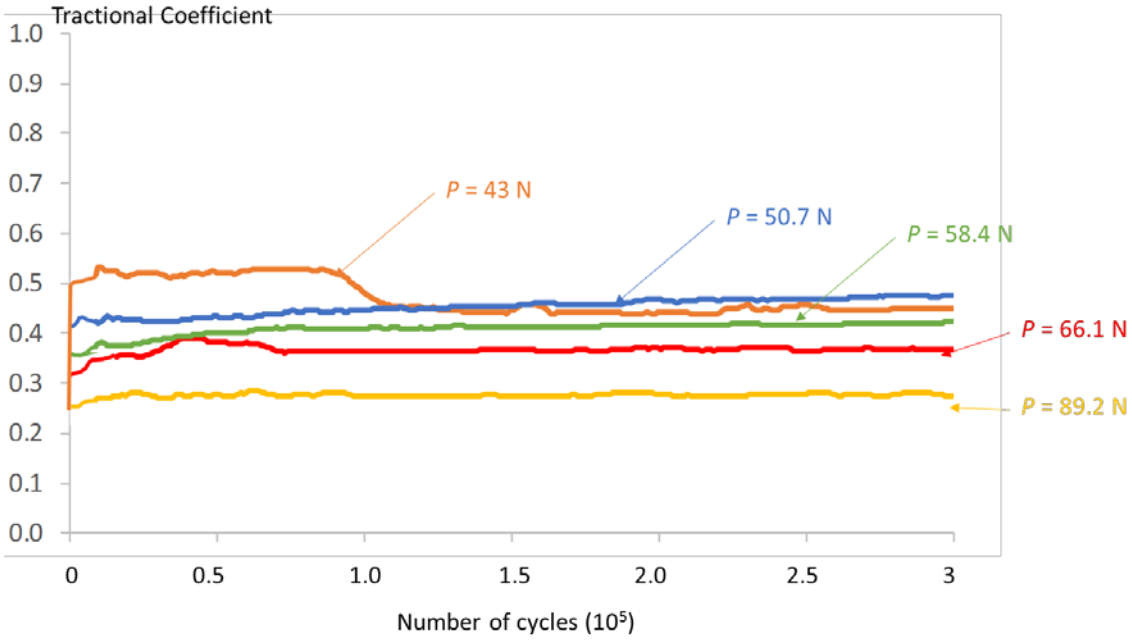

(b)

Figure 7. Measured evolution of ECoF and traction coefficients with number of fretting cycles for specimen with normal load of *P* for (a) gross-slip (contact pressure between 890 and 1270 MPa), and (b) mixed and partial slip conditions (contact pressure between 1350 and 1730 MPa).

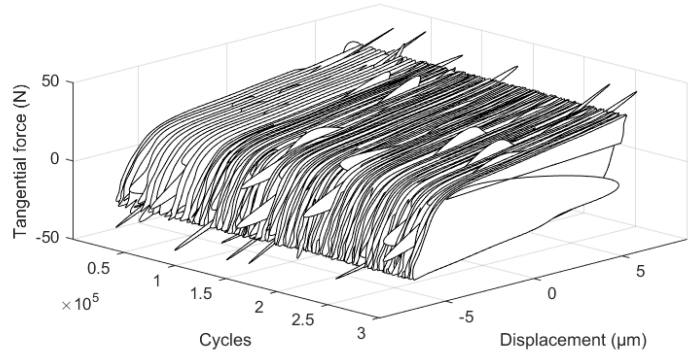

(a)

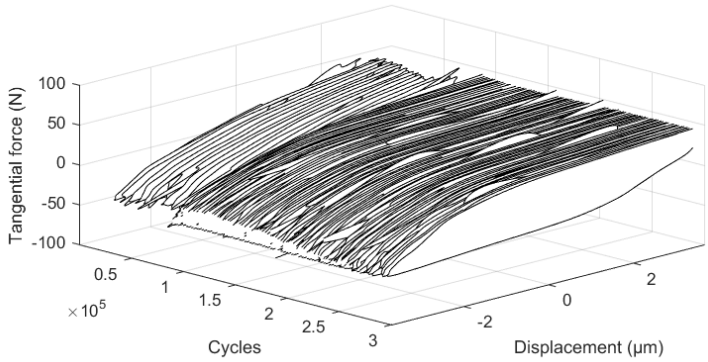

(b)

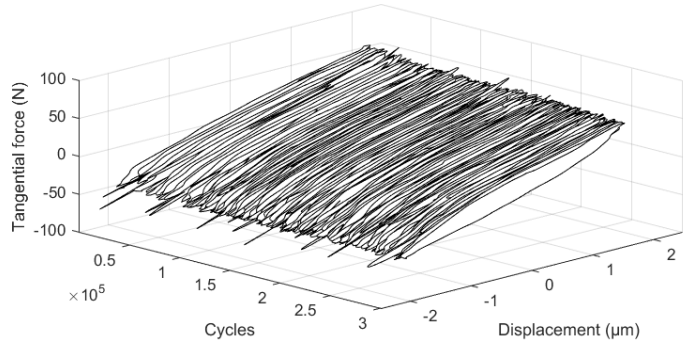

(c)

Figure 8. Measured evolution of fretting loop for tests with (a) gross slip conditions (contact pressure of 1270 MPa), (b) mixed slip conditions (contact pressure 1350 MPa), and (c) partial (contact pressure of 1600 MPa).

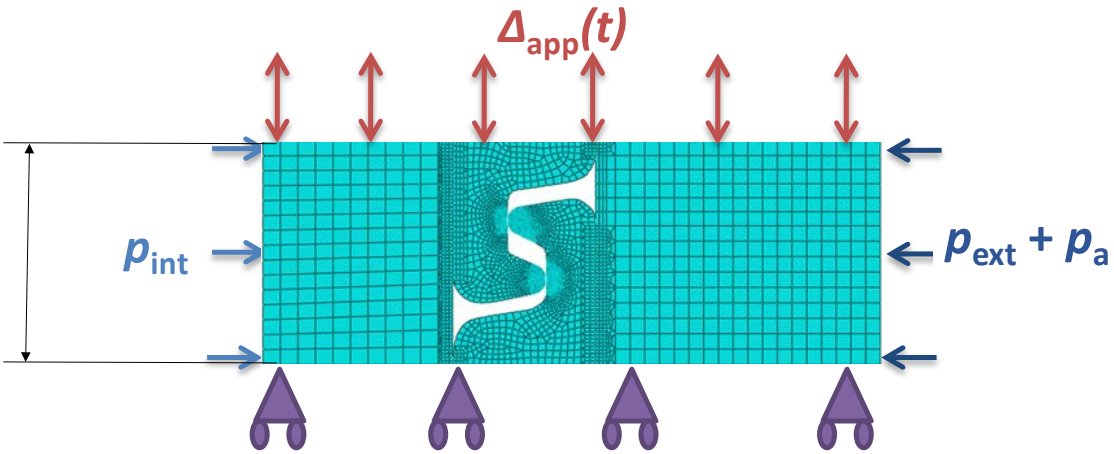

Figure 9. Axisymmetric riser model.

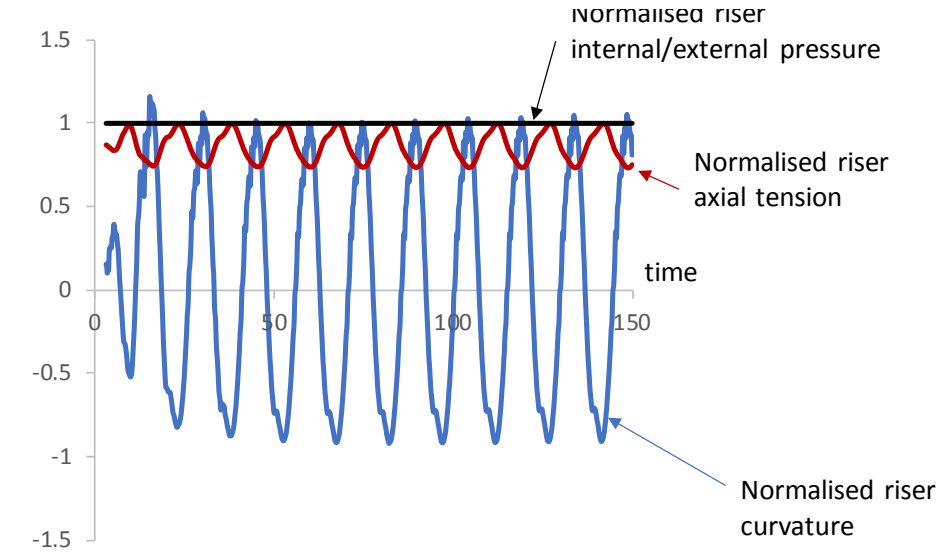

Figure 10. Time histories of normalised results from dynamic riser analysis.

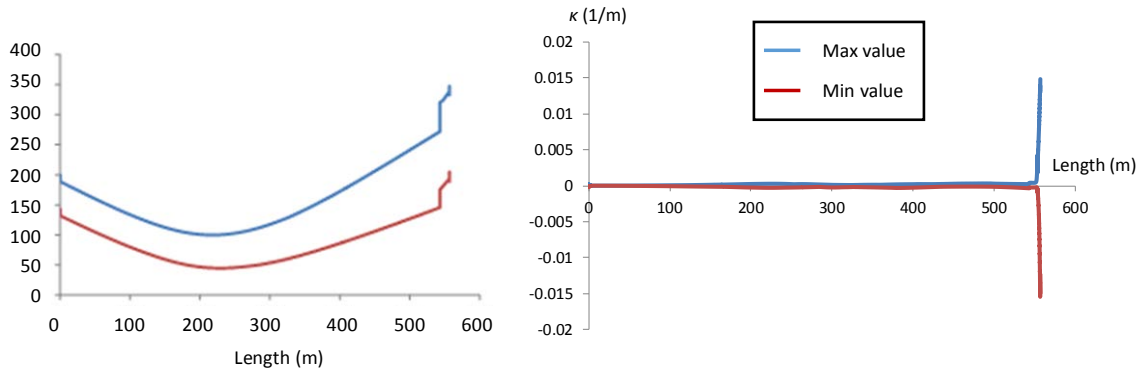

(a) (b)

Figure 11. Envelope of minimum and maximum (a) axial tensile force and (b) riser curvature along the length of the 6 inch riser jumper.

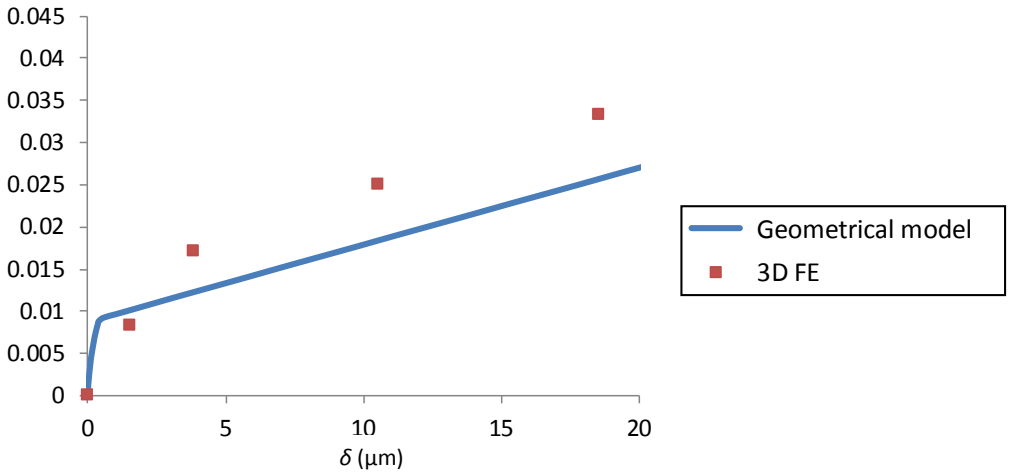

Figure 12. Comparison of geometrical and 3D FE models to obtain curvature-slip relationship for the 6 inch riser with nub-groove CoF of 0.7.

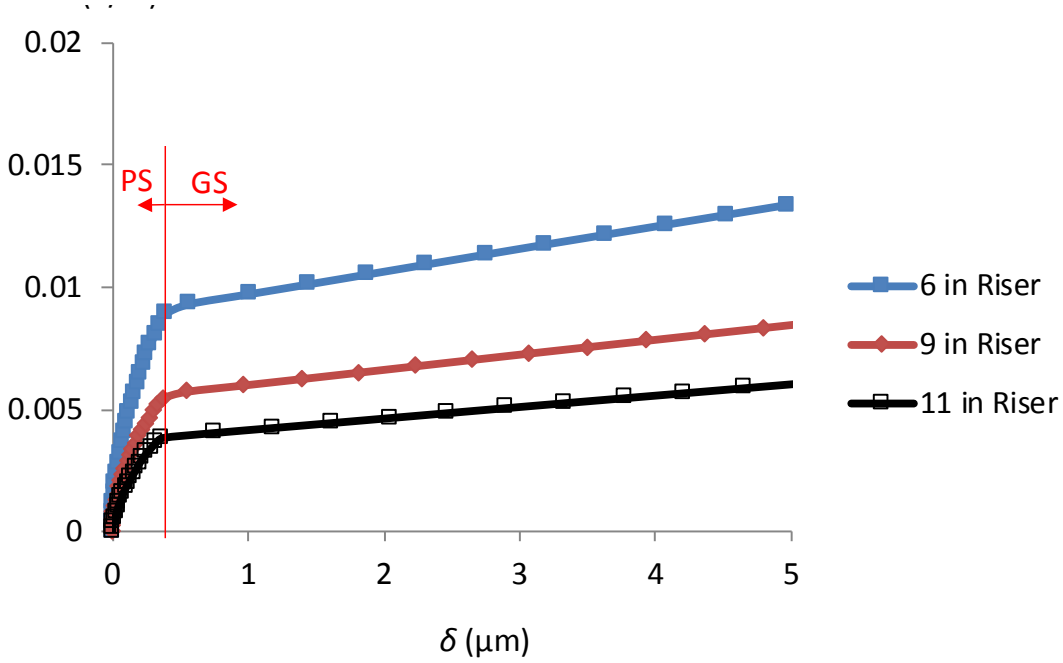

Figure 13. Curvature-slip relationship for the different risers used in this study.

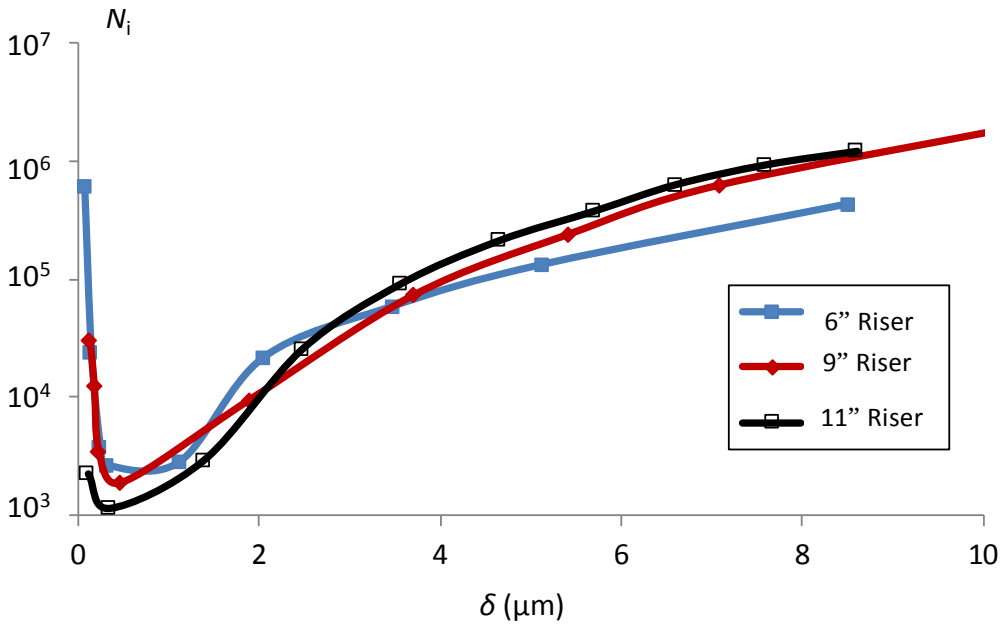

Figure 14. Number of cycles to crack initiation against nub-groove displacement for all three risers.

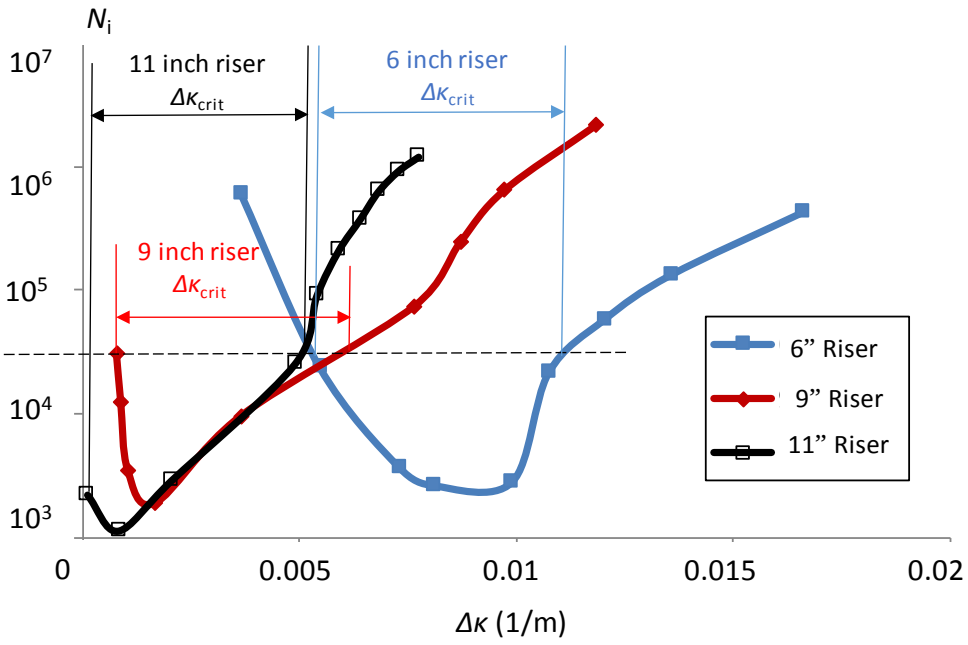

Figure 15. Number of cycles to crack initiation against dynamic riser curvature for all three risers and definition of $\Delta\kappa_{crit}$ for each riser case.

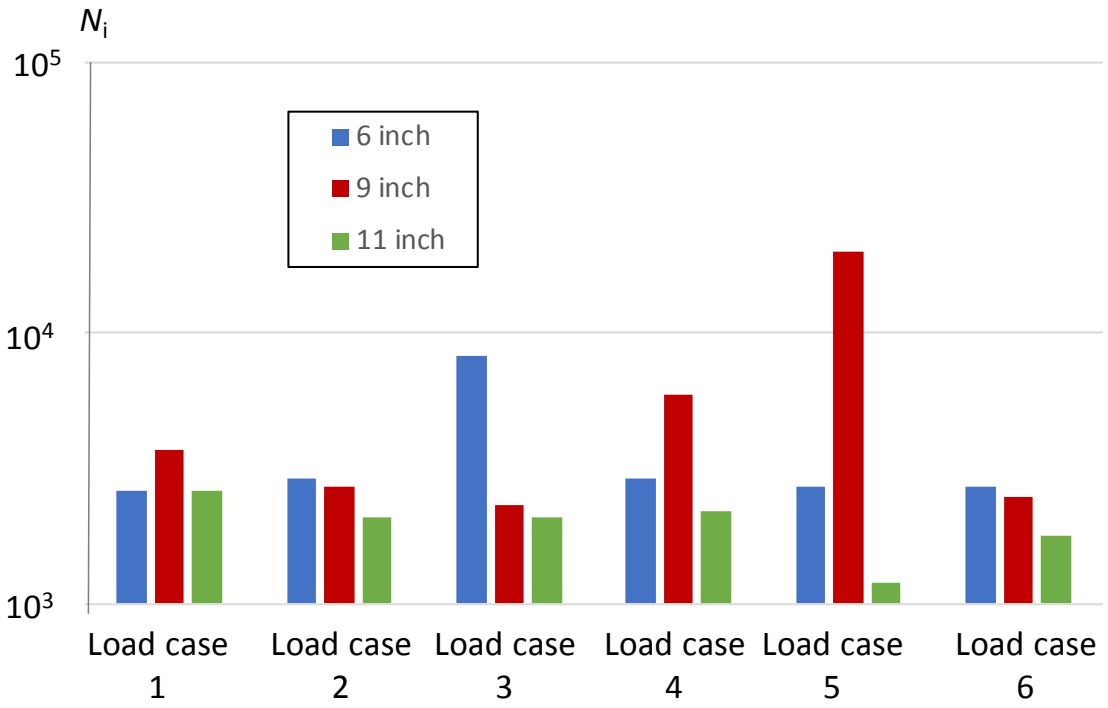

Figure 16. Predicted numbers of cycles to crack initiation for all load cases and all three risers.

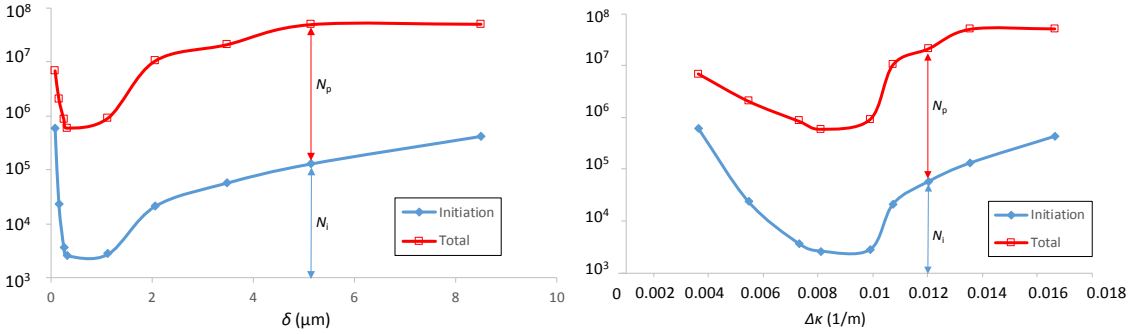

(a) (b)

Figure 17. Effect of (a) nub-groove contact slip and (b) global riser curvature on number of cycles to crack initiation and propagation for the 6 inch riser.

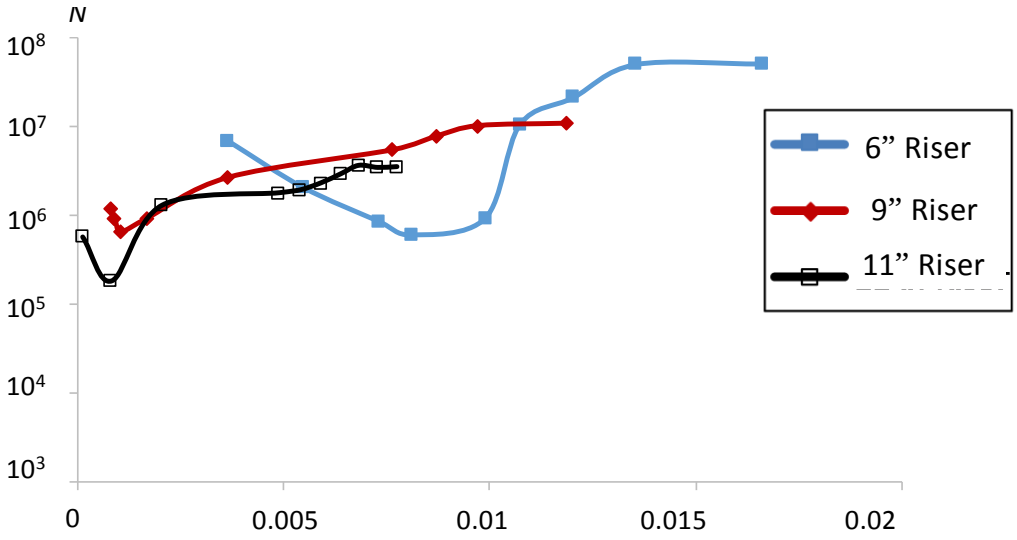

Figure 18. RCFM for predicted number of cycles to failure for dynamic curvature range for all three risers.

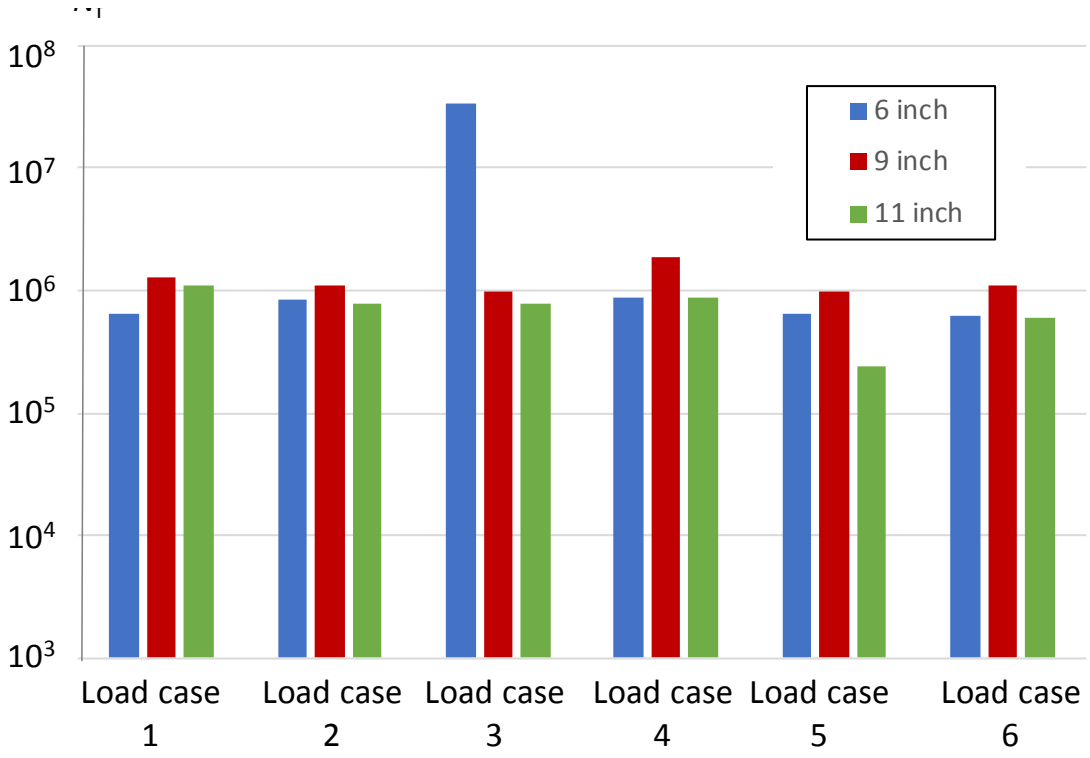

Figure 19. Predicted numbers of cycles to failure for all load cases and all three risers.